



Ultra-small colloidal heavy-metal-free nanoplatelets for efficient hydrogen generation

Haiguang Zhao^{a,**}, Hui Zhang^b, Guiju Liu^a, Xin Tong^{b,c}, Jiabin Liu^b, Gurpreet S. Selopal^{b,c}, Yiqian Wang^a, Zhiming M. Wang^c, Shuhui Sun^b, Federico Rosei^{b,c,*}

^a College of Physics & State Key Laboratory of Bio-Fibers and Eco-Textiles, Qingdao University, No. 308 Ningxia Road, Qingdao, 266071, PR China

^b INRS Centre for Energy, Materials and Telecommunications, 1650 Boulevard Lionel-Boulet, Varennes, Québec, J3X 1S2, Canada

^c Institute of Fundamental and Frontier Science, University of Electronic Science and Technology of China, Chengdu, 610054, PR China

ARTICLE INFO

Keywords:

Nanoplatelets
SnSe
Cation exchange
Hydrogen generation
Optoelectronic technologies

ABSTRACT

Metal chalcogenide semiconducting nanoplatelets exhibit a broad absorption spectrum, as well as thickness-dependent optical and electronic properties. As such, they may be used as building blocks in a variety of optoelectronic devices. The direct synthesis of heavy-metal-free ultra-small sized nanoplatelets is still challenging, due to the inherent limits in existing synthetic approaches. Here, we report an efficient template-assisted cation-exchange route to synthesize heavy metal free metal chalcogenide nanoplatelets that are optically active in the near infrared. The SnSe nanoplatelets, whose lateral dimension is 6–10 nm, exhibit a quantum yield of 20%. The nanoplatelets are applied as light absorbers in a photoelectrochemical (PEC) system for hydrogen generation, leading to a saturated photocurrent density of 7.4 mA/cm², which is a record for PEC devices using heavy metal-free colloidal quantum dots or nanoplatelets under identical measurement conditions. Our results indicate that quasi-zero-dimensional SnSe nanoplatelets hold great potential as efficient light absorbers for emerging optoelectronic technologies.

1. Introduction

Colloidal low-dimensional semiconducting nanocrystals are promising building blocks for solar technologies, such as solar cells, luminescent solar concentrators and solar-driven hydrogen (H₂) generation [1–8]. In particular, ultrathin two-dimensional (2D) nanocrystals, having sheet-like structures with few nanometers thickness have been used to fabricate optoelectronic devices [solar cells and photoelectrochemical (PEC) devices] [9–16]. Among various types of nanocrystals, nanoplatelets (NPLs) exhibit strong quantum confinement in one dimension, with wide absorption spectrum, relatively large absorption coefficient, high carrier mobility, high surface area and unique thickness-dependent optical and thermal properties [9–16]. Various types of colloidal NPLs including CdSe, CdSeS, CuInS, PbS, PbSeS, SnSe, SnS, In₂Se₃ etc have been recently synthesized through exfoliation method or other wet-chemical approaches [13–20]. Typically, the lateral dimension of NPLs is in the range of several tens of nanometers, up to several microns [13–20]. The large lateral dimension of NPLs complicates their deposition into mesoporous metal oxide thin films. More

importantly, NPLs with large dimension exhibit narrow bandgap [15], leading to unfavorable energy levels for efficient charge transfer from the NPLs to the metal oxide. Until now, these drawbacks have limited their use in optoelectronic devices.

To date, one of the most efficient methods to tailor the band energy structure is to synthesize ultra-thin NPLs with thickness less than a few layers. Although the synthesis of few layers or even one layer NPLs has been reported [18,21,22], the controlled synthesis of few layer metal chalcogenide NPLs using a simple approach still remains a great challenge. Another possible method to tune the band gap is to synthesize quasi zero-dimensional (0D) NPLs with three-dimensional (3D) quantum confinement, similar as quantum dots (QDs). However, due to the lack of available wet-chemistry synthetic approaches, there is still no report for directly preparing small-sized NPLs (lateral dimension < 10 nm) [13–20]. Recently, a two-step template-assisted cation exchange method was used to produce NPLs [15,17]. However, the obtained product contains heavy toxic metal Pb or Hg [15,17]. Up to now, although large sized NPLs have been realized [15–22], the synthesis of ultra-small sized quasi-0D heavy-metal free metal chalcogenide NPLs

* Corresponding author at: INRS Centre for Energy, Materials and Telecommunications, 1650 Boulevard Lionel-Boulet, Varennes, Québec, J3X 1S2, Canada.

** Corresponding author at: College of Physics & State Key Laboratory of Bio-Fibers and Eco-Textiles, Qingdao University, No. 308 Ningxia Road, Qingdao, 266071, PR China.

E-mail addresses: hgzhaoo@qdu.edu.cn (H. Zhao), Rosei@emt.inrs.ca (F. Rosei).

<https://doi.org/10.1016/j.apcatb.2019.03.028>

Received 14 December 2018; Received in revised form 28 February 2019; Accepted 11 March 2019

Available online 14 March 2019

0926-3373/ © 2019 Elsevier B.V. All rights reserved.

has yet to be reported.

Near infrared (NIR) heavy metal free tin chalcogenides (such as a narrow band gap SnSe, composed of environmentally friendly and earth abundant elements) enable a thickness/dimension/chemical composition-tunable wide absorption spectrum, ranging from ultra-violet (UV) to NIR, thereby significantly overlapping with the solar spectrum [18,19,22,23]. Until now however, high efficiency PEC devices based on NIR nanocrystals are exclusively composed of heavy-metal elements (e.g. Pb) [1,2]. SnS NPLs have been directly grown on fluorine doped tin oxide (FTO) substrates through a simple wet-chemical method and used as light absorber for PEC H₂ generation [24]. Due to the larger size of 2D NPLs (20 nm in thickness and 1.5 μ m in lateral dimension), the obtained saturated photocurrent density (*J*) of 1.2 mA/cm² [24] is still ten times lower than other typical photoanodes using colloidal 0D QDs [2].

Here, we report an efficient template-assisted cation-exchange route to synthesize ultra-small quasi-0D metal chalcogenide NPLs which are optically active in the NIR. The as-obtained NPLs have lateral dimensions less than 10 nm. As proof-of-concept, we then used the NPLs as photosensitizers for PEC H₂ generation. We obtained a saturated *J* of ~7.4 mA/cm² in a SnSe NPLs based PEC device, which is comparable to the performance of high-efficiency PEC devices based on heavy-metal nanocrystals. Our results indicate that ultra-small heavy-metal-free SnSe (or SnSe_xS_{1-x}) NPLs are a very promising candidate as green semiconductor building blocks for optoelectronic devices.

2. Experimental

2.1. Synthesis of metal chalcogenide NPLs

CdSe and CdSe_{1-x}S_x NPLs were synthesized by using a previously reported approach [14]. The as-prepared NPLs were dispersed in hexane for further characterization. Subsequently metal chalcogenide NPLs were obtained via a cation exchange method using CdSe and CdSe_{1-x}S_x NPLs as template [15,17]. Different metal halide precursors (GeCl₂, SnBr₂, PbBr₂, InCl₃, BiI₃ and HgCl₂) were used to replace Cd in the template. Typically, in a 50 mL round-bottom flask, the metal precursor (0.1–1 mmol), and oleylamine (OLA, 10 mL) were degassed at 100 °C for 10 min. The reaction flask was re-stored with nitrogen and the reaction temperature was raised to 120 °C while stirring for one hour. One milliliter of the CdSe or CdSe_{1-x}S_x NPLs suspension (0.05 mmol in hexane) was added slowly into the above reaction flask and the reaction mixture was stabilized at 120 °C for 10 min. Subsequently, oleic acid was added to the mixture when the temperature of the mixture decreased to 80 °C. After 20 min, the reaction was cooled to room temperature using cold water. Ethanol was added, then the suspension was centrifuged and the supernatant was removed. The NPLs were then dispersed in toluene for further characterizations.

2.2. Preparation of NPLs/TiO₂ film

NPLs/TiO₂ film was prepared by using a Doctoral-Blende approach [2,15]. A thin TiO₂ layer was spin coated on fluorine doped tin oxide (FTO) glass at 6000 rpm for 30 s by using the commercial solution Ti-Nanoxide BL/SC (Solaronix). Subsequently the films were annealed in air at 500 °C for 30 min after drying and cooled down to room temperature. A blend of active anatase particles (~20 nm) and larger anatase particles (up to 450 nm) paste (18 NR-AO, Dyesol) were tape casted on the FTO glass coated with a TiO₂ blocking layer, forming a mesoporous film. Then the film was annealed in air at 500 °C for 30 min. The NPLs were then deposited into TiO₂ film by electrophoretic deposition (EPD). Subsequently, a NPLs based TiO₂ film (photoanode) was dipped in hexadecyltrimethylammoniumbromide (CTAB)/methanol solution (10 mg/mL) for 30 s. The photoanode was rinsed with methanol for 1 min. This procedure was repeated three times. Subsequently, the photoanode was kept at 150 °C for 20 min under vacuum

conditions. Finally, two cycles of ZnS were coated on the photoanode using a successive ionic layer adsorption and reaction (SILAR).

2.3. Characterization

X-ray diffraction (XRD) analysis was performed on a Philips X'pert diffractometer using a Cu-K α radiation source (λ = 0.15418 nm). Transmission electron microscopy (TEM) was performed using a JEOL 2100 F TEM equipped with selected area electron diffraction (SAED) and energy dispersive X-ray spectroscopy (EDS). X-ray Photoelectron Spectroscopy (XPS) was performed in a VG Escalab 220i-XL equipped with a hemispherical analyzer. Inductively coupled plasma optical emission spectrometry (ICP-OES) (Agilent) was used to measure the molar ratio of Cd and Sn. Absorption spectra were acquired with a UV-2600 UV-vis spectrophotometer (Shimadzu). Fluorescence spectra were acquired with a FLS980 (Edinburgh). The PL lifetimes of the NPLs were measured using a pulsed laser diode of 440 nm and time-correlated single photon counting (TCSPC) mode in the FLS980 system. The quantum yield (QY) of SnSe and SnS_{0.5}Se_{0.5} NPLs was measured using Rhodamine 6 G as a reference.

2.4. PEC measurements

The PEC performance of the photoelectrodes fabricated using SnSe, SnS_{0.5}Se_{0.5}, Bi₂Se₃, CdSe, HgSe and PbSeS was evaluated in a three-electrode configuration, consisting of a NPLs-TiO₂ working electrode, a Pt counter electrode, and a KCl saturated Ag/AgCl reference electrode. Then the sample was immersed in the electrolyte (pH = 13, 0.25 M Na₂S and 0.35 M Na₂SO₃). All potentials were measured with respect to Ag/AgCl during the PEC test using a Metrohm Autolab (PGSTAT302N) and were converted to the RHE scale with the following expression $V_{\text{RHE}} = V_{\text{Ag/AgCl}} + 0.197 + \text{pH} \times 0.059$. The photoresponse was measured using an Oriel LCS-100 solar simulator (AM1.5 G). The light intensity measured using a power meter was ~100 mW cm⁻². The working area of the photoanode was ~0.12 cm². The *J* as a function of time was measured at 0.6 V vs. RHE under continuous AM 1.5 G illumination. H₂ evolution was measured during the PEC experiment. The produced H₂ gas was detected using a Shimadzu GC-8A gas chromatograph (GC) equipped with a thermal conductivity detector. Argon was used as carrier gas for GC analysis [2]. Detailed information about the calculation of the hydrogen generation rate is included in the Supporting information. Electrochemical impedance spectroscopy (EIS) of as-prepared SnSe NPLs/ZnS anode in the dark and under illumination (AM 1.5 G, 100 mW/cm²) was performed in FRA potentiostatic mode at the open circuit potential of 0.2 V vs. RHE and a scanning frequency from 10 kHz to 10 mHz. The EIS data was fitted using the NOVA software. The thickness of the anode is 5 μ m and the EPD time for SnSe NPLs deposition was 30 min.

3. Results and discussion

3.1. Synthesis and structure of NPLs

A two-step approach was used to synthesize small-sized metal chalcogenide NPLs [15]. First, we synthesized CdSe and CdSe_xS_{1-x} NPLs with average size over ~20 × 60 nm² and thickness of ~1.7 nm (Figs. 1a, d and S1), corresponding to ~5 monolayers (MLs). Typically, the as-prepared CdSe and CdSe_xS_{1-x} NPLs have a zinc blende (ZB) structure as confirmed by XRD patterns and SAED (Figs. S2–S3), consistent with previous work [14,15]. In addition, the *d* spacing of CdSe_xS_{1-x} NPLs in lateral dimension is measured to be ~3.45 Å, which is in between the *d* spacing of (111) plane for ZB structure of CdSe (JCPDS: 19-0191) and CdS (JCPDS: 75-0581) [15]. In the alloyed NPLs, the Se/S ratio with feeding ratios of Se/S equal to 1:1 is estimated as 1:1 from EDS. To adequately compare the effect of reaction conditions on the morphologies of cation exchanged NPLs, all the reactions, except the precursor

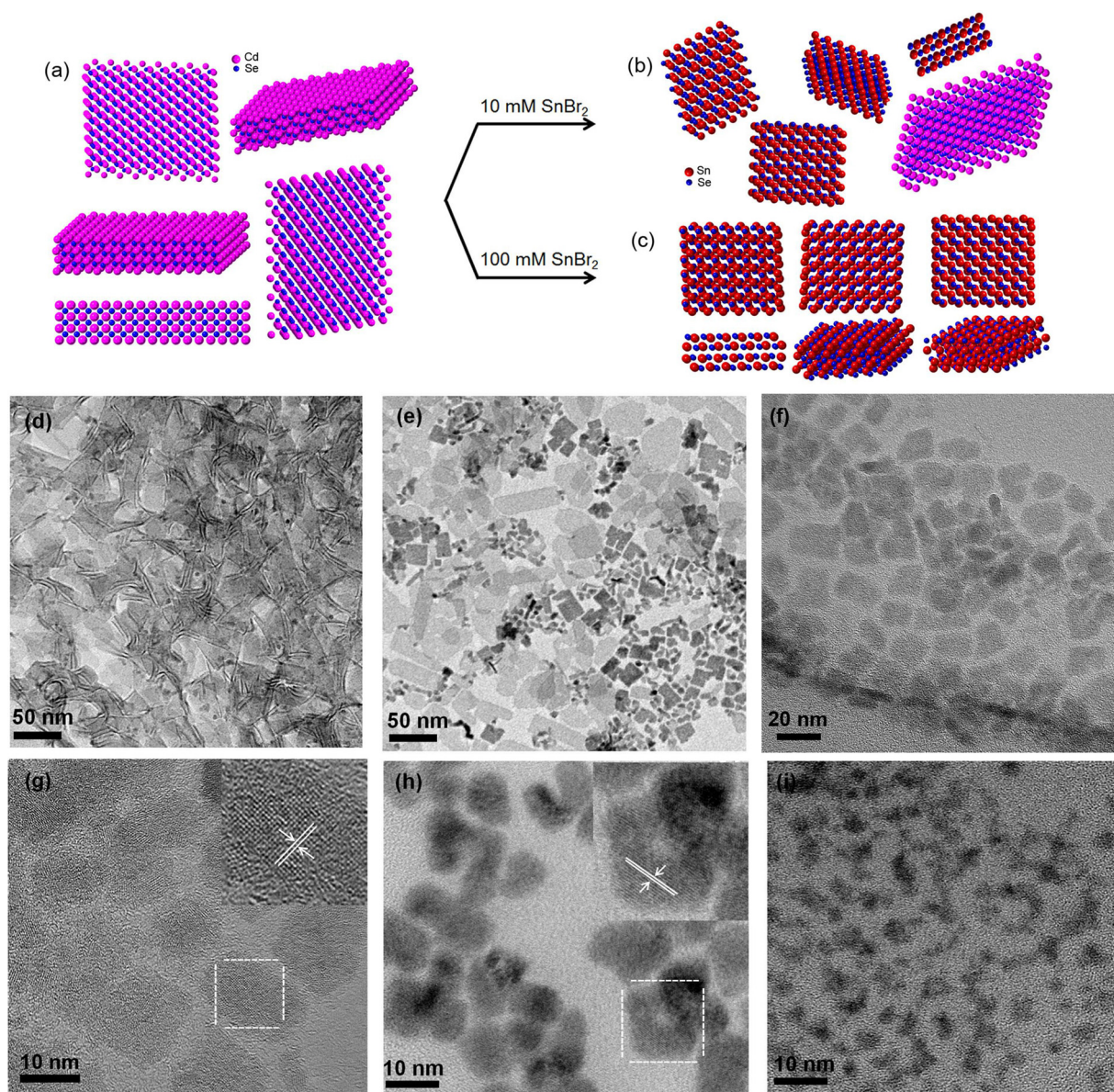


Fig. 1. (a–c) Scheme of the NPLs before and after cation exchange using different concentrations of SnBr_2 precursors [10 mM in (b) and 100 mM in (c)]. TEM of CdSe NPLs (d) and cation exchanged NPLs using SnBr_2 as precursor with concentration of 10 mM (e) and 100 mM (f). High magnification TEM of SnSe (g), SnSeS (h) and Bi_2Se_3 NPLs (i). The inset in g and h are the corresponding HRTEM images of NPLs.

concentration and the reaction temperature, were conducted under identical reaction conditions, such as precursor injection rate, reaction time and concentration of the template in hexane.

To investigate the crystalline structure of NPLs after cation exchange at different reaction conditions, we used Transmission Electron Microscopy (TEM) and high resolution TEM (HRTEM) (Fig. 1d–i). With the concentration of 10 mM SnBr_2 in OLA (the molar ratio of $\text{SnBr}_2/\text{CdSe}$ is 2), a mixture composed of CdSe NPLs, small and large sized SnSe NPLs was found (Fig. 1b and e). In contrast, with the concentration of 100 mM SnBr_2 in OLA (the molar ratio of $\text{SnBr}_2/\text{CdSe}$ is 20), only one type of small sized SnSe was found in the product (Fig. 1c and f). The high molar ratio of $\text{SnBr}_2/\text{CdSe}$ is favorable for the complete cation exchange reaction. A similar phenomenon was also found and confirmed by EDS data in the reaction system using $\text{CdSe}_x\text{S}_{1-x}$ NPLs as template (Fig. S4). The detailed correlation between the reaction conditions and product is shown in Table S1. Under certain reaction conditions, small-sized SnSe, SnSeS, Bi_2Se_3 , PbSeS, and HgSe were obtained (Figs. 1d–i, and S5–S6), but not for GeSe and In_2Se_3 NPLs (Fig.

S7a–c). EDS, ICP-OES and XPS confirmed a complete cation exchange between Cd and Sn in 100 mM samples (Fig. S1, 4, 8–10). Based on the EDS of a single NPL shown in Fig. S8, only the Sn signal was detected, confirming complete cation exchange between Cd and Sn (or Bi). As shown in Fig. S9, high-resolution XPS peaks at 404.5 eV and 411.3 eV correspond to Cd $3d_{5/2}$ and Cd $3d_{3/2}$ orbitals, respectively, whereas XPS peaks at 485.7 eV and 494.2 eV correspond to the Sn $3d_{5/2}$ and Sn $3d_{3/2}$ orbitals, respectively (Fig. S10). XPS analysis identifies the presence of residual Cd in $\text{SnSe}_x\text{S}_{1-x}$ and SnSe samples obtained using 10 mM precursors. No Cd was found in the samples obtained using 100 mM precursors, indicating a complete cation exchange between Cd and Sn, consistent with EDS data (Fig. S8) and ICP-OES measurement.

The cation exchange on CdSe (or CdSeS) NPLs using various metal halide precursors induces the formation of different ultra-small NPLs (Figs. 1g–i and S6.). All NPLs exhibit smaller size (less than 20 nm) than the starting CdSe or $\text{CdSe}_{1-x}\text{S}_x$ NPLs (Figs. 1d and S1). By rotating the angle between the sample holder and the e-beam during TEM measurement, the NPLs exhibit angle-dependent morphologies, due to the

irregular shape of NPLs (Fig. S11). Together with HRTEM of NPLs, TEM imaging confirms the 2D structure in as-obtained nanocrystals. The SnSe, SnSeS, Bi₂Se₃, and PbSe NPLs exhibit a broad size distribution with average lateral dimensions between ~4–20 nm. HgSe NPLs exhibit an irregular shape with lateral dimension greater than 20 nm (Fig. S6a). SAED and XRD indicate the typical cubic phase and alloyed composition in SnSe_{1-x}S_x NPLs (Fig. S5a,c), consistent with the calculated $d_{(200)}$ spacing of ~2.98 Å which is in between the $d_{(200)}$ spacing of cubic SnSe and SnS (Fig. 1h). Similarly, the calculated d spacing of ~3.04 Å in SnSe NPLs is consistent with the (011) plane of the orthorhombic structure (Figs. 1g, Fig. S5c and S12). The CdSe NPLs obtained after cation exchange using BiBr₃ as precursor exhibit a typical rhombohedral structure, confirming the formation of Bi₂Se₃ NPLs (Fig. S5b,d). As reported in the literature, there is no significant change of the dimensional size of HgSe NPLs before and after cation exchange conducted at 25 °C for 12 h using CdSe NPLs as template [17]. In our case, as the reaction temperature is around 120 °C, the strong etching effect explains the formation of small-sized NPLs [15,25]. During the cation exchange process, the template NPLs were fragmented due to either the higher surface energy of their polycrystalline structure or strong reactivity of the precursors at relatively high reaction temperatures.

3.2. Optical properties of NPLs

After cation exchange the absorption spectra of SnSe and SnSe_{1-x}S_x absorb from 400 to 1000 nm without an obvious first-excitonic absorption peak (Fig. 2a–b), which is a typical behaviour for SnSe nanocrystals [23]. The photoluminescence (PL) peak of SnSe NPLs is located at 842 nm and that of SnSeS is located at 865 nm (Fig. 2b), which is largely red-shifted compared to that of CdSe or CdSeS NPLs (Fig. 2a). The different PL peaks between SnSe and SnSeS NPLs may be due to their different chemical composition, size and thickness. The QY of SnSe NPLs in hexane is around 20%, similar to the QY of templated CdSe and CdSeS NPLs, which is five times higher than that of SnSeS NPLs. The lower QY in SnSeS NPLs is consistent with its shorter lifetime (510 ± 10 ns) compared with that of SnSe NPLs (870 ± 10 ns) (Fig. 2c). The alloyed CdSeS contains many grain boundaries, which are very active during the cation exchange reaction, inducing more surface recombination centers in SnSeS NPLs than that in SnSe NPLs [15]. These recombination centers lead to non-radiative decay events in the SnSeS NPLs, explaining both its low QY and short lifetime. The SnSe NPLs with high QY, long lifetime and NIR emission window (700–1000 nm) represent an excellent candidate for deep-tissue bioimaging, bio-sensing and optoelectronic devices [1–3,26,27].

In general, SnSe bulk materials have an indirect bandgap around

0.9 eV as reported previously [25]. With the increase of nanocrystal size from 3 to 10 nm, the bandgap of SnSe nanocrystals decreases from 1.25 eV to 0.9 eV, and confinement effects taper off near 10 nm [25]. In the present case, if the as-obtained nanocrystals have sizes between 6–10 nm, based on previous work [25], the bandgap should be lower than 1.25 eV. Surprisingly however, the estimated bandgap based on the emission band is ~1.47 and 1.43 eV for SnSe and SnSeS NPLs, respectively. This value should be even lower than that of the real bandgap in NPLs as the emission band is usually lower than the band gap of nanocrystals due to the Stokes shift. In fact, for five layered SnSe platelets (lateral dimension > 1 μm), the bandgap was reported to be around 1.2–1.4 eV [28]. The wider bandgap suggests that the as-prepared NPLs exhibit quantum confinement mainly in one dimension (thickness-dependent quantum confinement), as also found in small-sized PbSe or PbSeS NPLs [15].

The typical emission peak of Bi₂Se₃ NPLs is in the NIR (~1200 nm) (Fig. S12). Compared with the high QY in SnSe NPLs, Bi₂Se₃ NPLs have a very low QY of 1% because of surface defects, due to the strong etching effect by BiBr₃/OLA precursors. This etching effect was also confirmed by the emission spectrum of CdSe NPLs after treatments using InCl₃/OLA, leading to a very broad emission other than narrow emission band of original NPLs (Fig. S14).

3.3. PEC performance of NPLs based photoanode

The calculated bandgaps of SnSe NPLs and band energy levels are presented in Fig. 3. These values are favorable for charge transfer from NPLs to TiO₂, as well as for water reduction (H₂/H₂O: -0.7 eV vs. normal hydrogen electrode (NHE)) [29]. This is due to its ultra-small size which is under quasi-3D confinement, enabling to tune their electronic states and PL emission. Other metal chalcogenide NPLs also exhibit a favorable band alignment between the semiconductor conduction band and the energy level for water reduction. Due to the unfavorable energy levels of the valence band in the PbS and Bi₂Se₃, these materials are not suitable for water splitting, but photogenerated holes in these materials can transfer to hole scavengers (S²⁻/SO₃²⁻) (Fig. 3). As proof-of-concept, we used these quasi-0D ultra-small nanocrystals for PEC hydrogen generation. Compared with Cd and Pb based QDs or NPLs, SnSe and SnSeS are environmentally friendly without containing toxic elements. In addition, the as-prepared NPLs exhibit a broad absorption range up to the NIR, which is wider than SnS and In₂Se₃ nanocrystals [19,20,24,30].

For the anode preparation, a typical thickness of TiO₂ mesoporous film is around 18 μm, using a doctor-blade approach [15]. The PEC performance of the NPLs was measured by a three electrode system

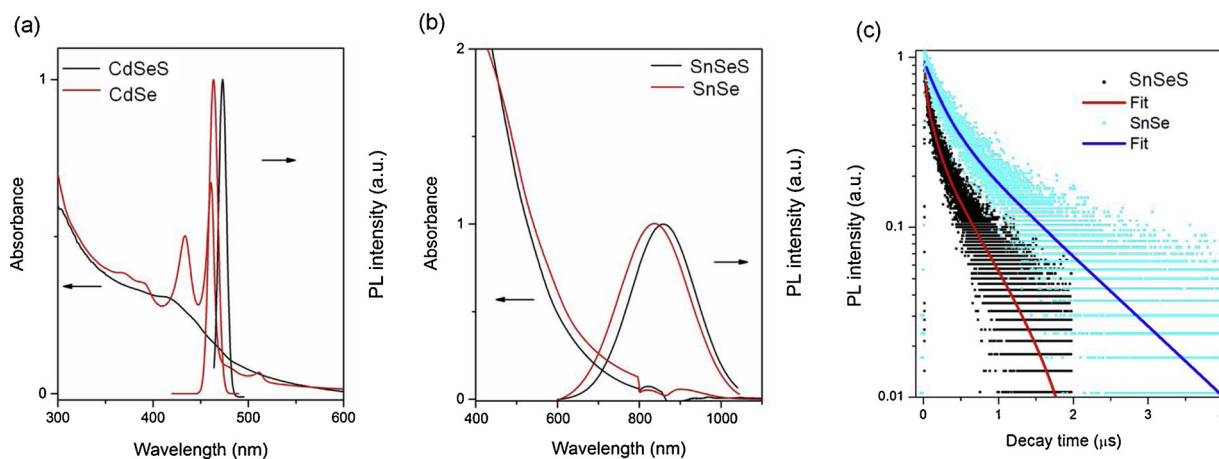


Fig. 2. (a) Absorption and PL spectra of parent CdSe and CdSe_{1-x}S_x NPLs. (b) Absorption and PL spectra of SnSe and SnSe_{1-x}S_x NPLs. The excitation wavelength is 400 nm for all NPLs dispersed in toluene. (c) PL decay curves (dots) and fitting curves (solid lines) for SnSe and SnSe_{1-x}S_x NPLs measured at the emission peak in toluene, shown on a semi-logarithmic scale. The excitation wavelength was set at 450 nm.

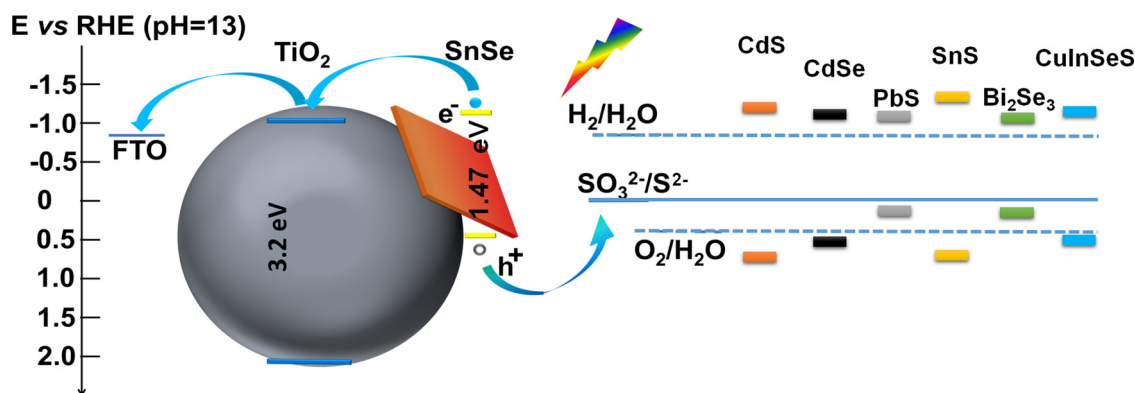


Fig. 3. Schematic diagram and approximate band alignment of NPLs-sensitized photoanodes.

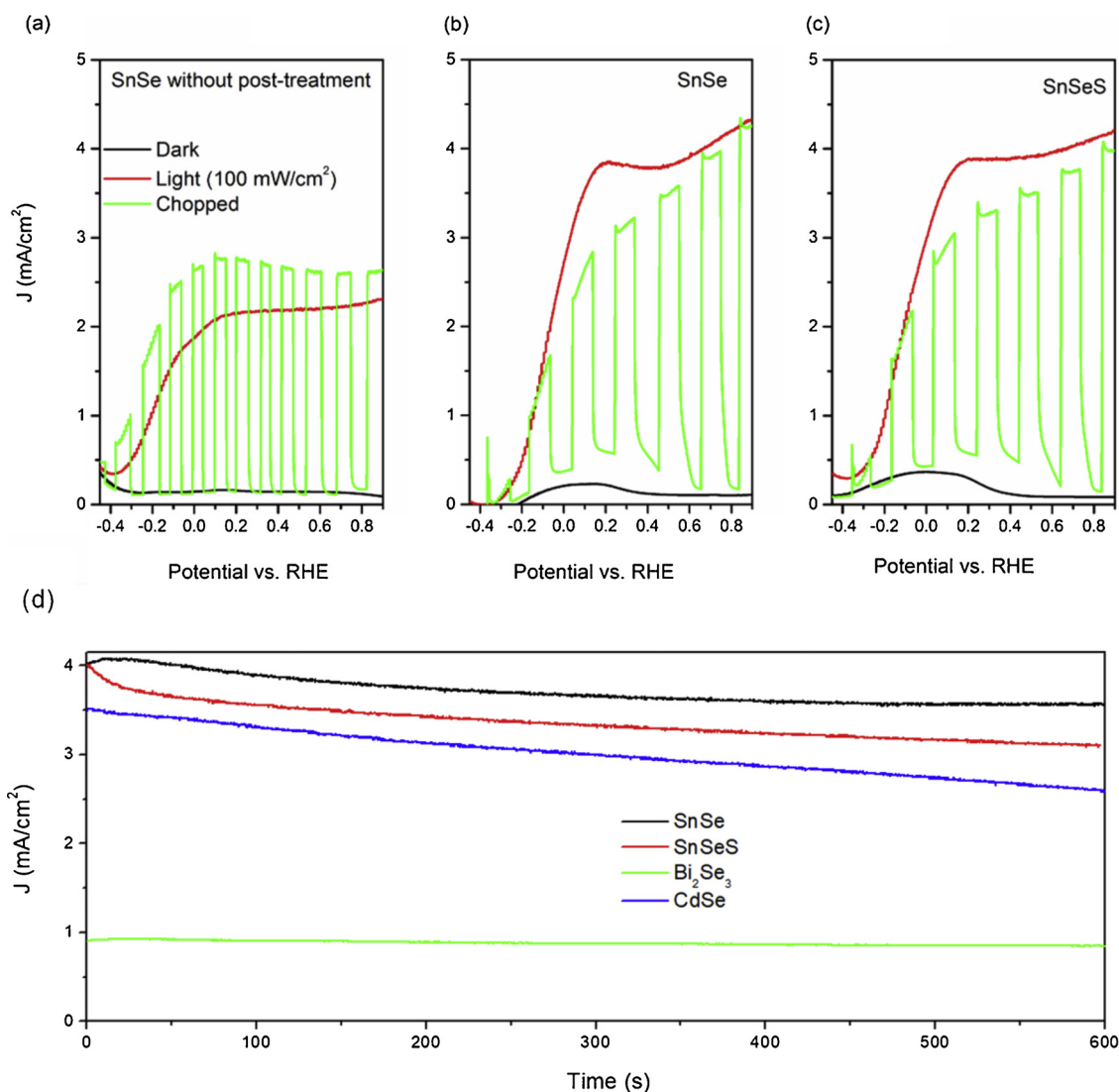


Fig. 4. (a–c) J - V (versus RHE) of NPLs/TiO₂-sensitized photoelectrodes in the dark (black curve), under continuous (red curve) and chopped (green curve) illumination (AM 1.5 G, 100 mW/cm²). SnSe NPLs before (a) and after (b) post-treatment and SnSeS NPLs. (d) J as a function of time of NPLs/TiO₂-sensitized anodes at 0.6 V versus RHE under AM 1.5 G irradiation (100 mW/cm²). (For interpretation of the references to colour in this figure legend, the reader is referred to the web version of this article.)

[Metrohm Autolab (PGSTAT302 N)] and demonstrated in Fig. 4a–c. The PEC device based on bare TiO₂ exhibits a saturated current density of 0.3 mA/cm² as the TiO₂ can only absorb sunlight in the range 300–400 nm [32]. A value of saturated J of ~0.8 mA/cm² was reported for pure PbSe NPLs treated with Cd cations at 40 °C [15]. Other than

strong surface oxidation during anode preparation in the system of PbSeSe NPLs [15], the PEC device based on SnSe NPLs without post-thermal treatment exhibits a saturated J of ~2.1 mA/cm² (Fig. 4a). When illuminating the anode with chopped light, the saturated J increases to ~2.6 mA/cm² (Fig. 4b), which is more than 2 times higher

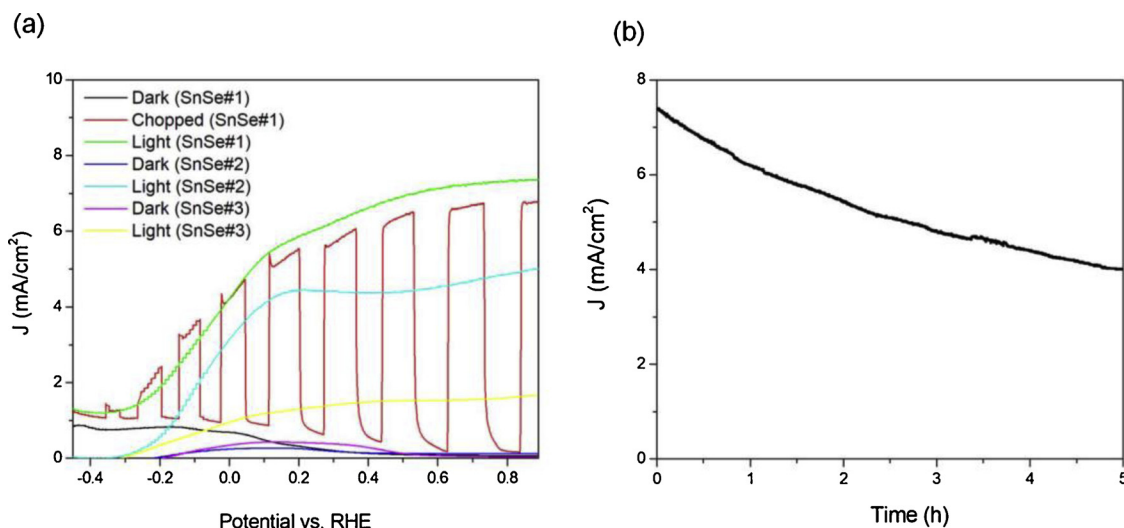


Fig. 5. (a) J - V (versus RHE) of SnSe NPLs/ TiO_2 sensitized photoelectrodes in the dark (black curve) and under continuous (red curve) illumination (AM 1.5 G, $100 \text{ mW}/\text{cm}^2$). The anode was prepared using the following parameters: (#1) the thickness of TiO_2 film ($18 \mu\text{m}$) and the EPD time (0.5 h); (#2) the thickness of TiO_2 film ($18 \mu\text{m}$) and the EPD time (1 h); (#3) the thickness of TiO_2 film ($12 \mu\text{m}$) and the EPD time (1 h). All anodes were post-treated at 150°C for 30 min. (b) J as a function of time of NPLs/ TiO_2 -sensitized anodes using the parameters #2 at 0.6 V versus RHE under AM 1.5 G irradiation ($100 \text{ mW}/\text{cm}^2$). (For interpretation of the references to colour in this figure legend, the reader is referred to the web version of this article.)

than PbSeS NPLs and large SnSe platelet-based PEC devices under identical measurement conditions (same electrolyte and counter electrode, electrode size, light intensity, etc) [15,24].

Sunlight illumination can induce self-surface annealing, decreasing the number of recombination centers created during the anode preparation process [31]. In the following, before PEC measurements, all anodes were annealed at 150°C for 20 min to improve PEC device performance. Under one sun illumination ($100 \text{ mW}/\text{cm}^2$), the anode based on SnSe NPLs exhibits a saturated J of $\sim 4 \text{ mA}/\text{cm}^2$ at 0.6 V vs RHE (Fig. 4c). Similar values of saturated J were also found in the PEC device based on alloyed SnSeS NPLs (Fig. 4c). The obtained saturated J is much higher as opposed to values obtained using other NPLs (HgSe, Bi_2Se_3 , CdSe and CdSeS) based anodes under identical measurement apparatus and conditions (Fig. S15). Our obtained J value is also much higher than that of pure PbSeS NPLs or SnSe platelet-based anode [15,24]. With further optimization of the thickness of TiO_2 and the EPD time, the saturated J reaches $\sim 7.4 \text{ mA}/\text{cm}^2$ (Fig. 5a). This J is comparable to values reported from PEC systems using Cd or Pb based QDs or NPLs as light absorbers [35–40], such as PbS/CdS NPLs ($5 \text{ mA}/\text{cm}^2$) [15], PbS/CdS/CdS QDs ($11 \text{ mA}/\text{cm}^2$) [32], CdSe/CdS QDs ($10 \text{ mA}/\text{cm}^2$) [2], CdS and CdSe QDs-co-sensitized TiO_2 ($14.9 \text{ mA}/\text{cm}^2$) [33] and PbS and Mn-CdS QDs-co-sensitized TiO_2 ($22.1 \text{ mA}/\text{cm}^2$) [34]. However, these materials (QDs or NPLs) contain hazardous heavy metal ions. To the best of our knowledge, this is a record J at 0.8 V vs RHE for heavy-metal-free NIR QDs or NPLs based photoelectrodes for solar-driven PEC hydrogen generation (Table 1), such as large-sized SnSe

NPLs ($\sim 2.1 \text{ mA}/\text{cm}^2$) [24], CuInSeS/ZnS QDs ($\sim 5 \text{ mA}/\text{cm}^2$) [35], CuInSe/CuInS QDs ($\sim 3 \text{ mA}/\text{cm}^2$) [31], and carbon dots sensitized $\text{NiOOH}/\text{FeOOH}/\text{BiVO}_4$ ($5.99 \text{ mA}/\text{cm}^2$) [36] or carbon dots sensitized $\text{Ti}/\text{Fe}_2\text{O}_3/\text{graphitic carbon nitride}$ nanosheets ($3.38 \text{ mA}/\text{cm}^2$) [40]. This value is also comparable with that of PEC devices based on metal oxides, such as hematite ($3.05 \text{ mA}/\text{cm}^2$) [37] and Cu_2O nanowires ($10 \text{ mA}/\text{cm}^2$) [38].

We further measured the stability of anode (at 0.6 V vs RHE), finding an approximate drop of about 26% of the original current density after 600 s in the PEC device based on CdSe NPLs (Fig. 4d). This rapid decrease is probably due to the slow charge separation and transfer as the large-sized NPLs cannot adsorb effectively on the TiO_2 mesoporous structure. A similar behaviour was also found in the SnSeS based anode. On the other hand, the SnSe-based photoanode exhibits very good stability: 89% of its initial J was maintained after 600 s illumination. The good stability of the PEC device based on SnSe NPLs is mainly attributed to its excellent optical properties with respect to its high QY and long lifetime. In addition, the PEC device based on Bi_2Se_3 nanocrystals also exhibits very good stability, as 93% of its initial J was maintained after 600 s illumination. This performance is comparable to that of the best photoanodes previously reported [32–41]. Further stability measurements for the optimized anode based on SnSe NPLs with the preparation parameters (#1) indicate a decrease of J as a function of illumination time (Fig. 5b) and the J decreases to $4 \text{ mA}/\text{cm}^2$ after 5 h illumination. The reason for the decrease of J is mainly due to (i) chemical corrosion as the pH value of the electrolyte is 13; (ii) the photoinduced structure degradation; and (iii) the hole accumulation induced surface oxidation due to the slow hole transfer rate [32–40]. Further improving the stability of the PEC devices may focus on the replacement of alkaline electrolyte with neutral solution with the addition of hole acceptors.

Our work indicates that the Faraday efficiency is $\sim 80\%$, using Pt as counter electrode and $\text{Na}_2\text{S}/\text{Na}_2\text{SO}_3$ as electrolyte (Fig. S16). Based on the reference curve, we integrated the current density (Fig. 5b), and on this basis the calculated hydrogen generation rate of the PEC device based on SnSe NPLs is $\sim 42 \text{ mL}/\text{cm}^2 \cdot \text{day}^{-1}$, which is comparable to the values obtained using other materials [31,35,36,40].

In order to further understand the PEC reaction kinetics, the as-prepared SnSe NPLs/ZnS photoanode was investigated by EIS. Fig. S17 shows the Nyquist plots of the $\text{TiO}_2/\text{SnSe-NPLs}/\text{ZnS}$ photoanode- $\text{Na}_2\text{S}/\text{Na}_2\text{SO}_3$ electrolyte system for the EIS measurements performed in the

Table 1

Saturated J (mA/cm^2) in PEC devices based on various type of colloidal heavy-metal-free nanocrystals. The J was measured under $100 \text{ mW}/\text{cm}^2$ illumination in the presence of the electrolyte.

Anode	J (mA/cm^2)	Ref.
SnSe sensitized TiO_2	7.4	This work
Bi_2Se_3 sensitized TiO_2	1.0	This work
$\text{SnS}_x\text{Se}_{1-x}$ sensitized TiO_2	2.6	This work
CuInSeS/ZnS sensitized TiO_2	5	[35]
CuInSe/CuInS sensitized TiO_2	3	[31]
$\text{NiOOH}/\text{FeOOH}/\text{Carbon quantum dots}/\text{BiVO}_4$	5.99	[36]
Carbon dot sensitized $\text{Ti}/\text{Fe}_2\text{O}_3/\text{graphitic carbon nitride}$ nanosheets	3.38	[40]

dark and under illumination conditions (AM 1.5 G, 100 mW/cm²). Similar EIS features were found for the sample measured in the dark and under illumination, which are a semicircle arc at high frequency and a linear region at low frequency. Because the electronic processes in the bulk are normally faster than charge transfer processes or diffusion of ions in electrolyte, in our system, the low frequency response is assigned to the semiconductor-electrolyte charge transfer resistance (R_{ct}), and the high frequency response is assigned to events occurring in the semiconductor [42–44]. The spectra were modeled using a simplified electronic equivalent circuit (Fig. S17a) [42–44]. The circuit series resistance (R_s) is constant about 40–50 ohms for the system in the dark and under illumination. A smaller high frequency arc for the electrode under illumination compared to the electrode in the dark was found, indicating a decrease of R_{ct} from 730 to 590 ohms under illumination (Fig. S17b). This decreasing R_{ct} is due to the increased conductivity in the semiconductor afforded by illumination [42].

4. Conclusions and perspectives

In summary, we demonstrated a simple template-assisted cation exchange approach to synthesize metal chalcogenide NPLs optically active in the NIR, including SnSe, SnSeS and Bi₂Se₃ NPLs. The SnSe NPLs exhibit a lateral dimension of 6–10 nm with a QY of 20% and a fluorescence lifetime up to 870 ns, showing great potential for application in optical and electronic devices, such as solar cells and PEC hydrogen production. The SnSe NPL-based photoanode exhibits a saturated J of ~7.4 mA/cm² at 1.0 V vs RHE, which is six times higher than that of the large sized SnSe platelet and comparable with that of PEC device using heavy metal PbS/CdS NPLs under identical measurement conditions. In addition, PEC devices based on SnSe NPLs exhibit good photostability, observing that J still retained values of about 4 mA/cm² after 5 h illumination. Our results indicate that small-sized SnSe NPLs are promising as efficient light absorbers for optoelectronic devices. Future directions may focus on the development of SnSe NPLs with different thickness and small-sized core/shell structured SnSe/SnS or SnS/SnSe NPLs for optical and electronic devices.

Conflict of interest

The authors declare no conflict of interest.

Acknowledgements

H.G. Zhao acknowledges funding from the Natural Science Foundation of Shandong Province (ZR2018MB001) and start-up funds from Qingdao University. Z.M. Wang acknowledges the funding from the National Basic Research Program (973 Program) of China (No. 2013CB933301) and the Natural Science Foundation of China (No. NSFC-51272038). F.R. acknowledges funding from the Natural Science and Engineering Research Council of Canada (NSERC), the Canada Foundation for Innovation (CFI) for infrastructure support and its operating funds and the Fonds de recherche du Québec – Nature et technologies (FRQNT). F.R. thanks the Canada Research Chairs program for funding and partial salary support. F.R. acknowledges a Chang Jiang short term scholar award (government of China) and the Sichuan 1000 talents short term award.

Appendix A. Supplementary data

Supplementary material related to this article can be found, in the online version, at doi:<https://doi.org/10.1016/j.apcatb.2019.03.028>.

References

- [1] H. Zhao, F. Rosei, Colloidal quantum dots for solar technologies, *Chem.* 3 (2017) 229–258.

- [2] R. Adhikari, L. Jin, F. Navarro-Pardo, D. Benetti, B. Alotaibi, S. Vanka, H.G. Zhao, Z.T. Mi, A. Vomiero, F. Rosei, High efficiency, Pt-free photoelectrochemical cells for solar hydrogen generation based on “giant” quantum dots, *Nano Energy* 27 (2016) 265–274.
- [3] G. Selopal, H. Zhao, D. Benetti, X. Tong, F. Navarro-Pardo, Y. Zhou, D. Barba, F. Vidal, Z.M. Wang, F. Rosei, Highly stable colloidal “giant” quantum dots sensitized solar cells, *Adv. Funct. Mater.* 27 (2017) 1701468.
- [4] Y. Tachibana, L. Vayssieres, J.R. Durrant, Artificial photosynthesis for solar water-splitting, *Nat. Photon.* 6 (2012) 511–518.
- [5] J. Pan, S.M. Huhne, H. Shen, L.S. Xiao, P. Born, W. Mader, S. Mathur, SnO₂-TiO₂ core-shell nanowire structures: investigations on solid state reactivity and photocatalytic behavior, *J. Phys. Chem. C* 115 (2011) 17265–17269.
- [6] L.P. Heiniger, P.G. O'Brien, N. Soheilnia, Y. Yang, N.P. Kherani, M. Grätzel, G.A. Ozin, N. Tetreault, See-through dye-sensitized solar cells: photonic reflectors for tandem and building integrated photovoltaics, *Adv. Mater.* 25 (2013) 5734–5741.
- [7] N. Armario, V. Balzani, The future of energy supply: challenges and opportunities, *Angew. Chem.* 46 (2007) 52–66.
- [8] K.H. Liu, H.X. Zhong, S.J. Li, Y.X. Duan, M.M. Shi, X.B. Zhang, J.M. Yan, Q. Jiang, Advanced catalysts for sustainable hydrogen generation and storage via hydrogen evolution and carbon dioxide/nitrogen reduction reactions, *Prog. Mater. Sci.* 92 (2018) 64–111.
- [9] X.J. Wu, J.Z. Chen, C.L. Tan, Y.H. Zhu, Y. Han, H. Zhang, Controlled growth of high-density CdS and CdSe nanorod arrays on selective facets of two-dimensional semiconductor nanoplates, *Nat. Chem.* 8 (2016) 470–475.
- [10] C. Schliebe, B.H. Juarez, M. Pelletier, S. Jander, D. Greshnykh, M. Nagel, A. Meyer, S. Foerster, A. Kornowski, C. Klinke, H. Weller, Ultrathin PbS sheets by two-dimensional oriented attachment, *Science* 329 (2010) 550–553.
- [11] M. Aerts, T. Bielewicz, C. Klinke, F.C. Grozema, A.J. Houtepen, J.M. Schins, L.D.A. Siebbeles, Highly efficient carrier multiplication in PbS nanosheets, *Nat. Commun.* 5 (2014) 3789.
- [12] R.J. Ellingson, M.C. Beard, J.C. Johnson, P. Yu, O.I. Micic, A.J. Nozik, A. Shabaev, A.L. Efros, Highly efficient multiple exciton generation in colloidal PbSe and PbS quantum dots, *Nano Lett.* 5 (2005) 865–871.
- [13] H.T. Zhang, B.H. Savitzky, J. Yang, J.T. Newman, K.A. Perez, B.R. Hyun, L.F. Kourkoutis, T. Hanrath, F.W. Wise, Colloidal synthesis of PbS and PbS/CdS nanosheets using acetate-free precursors, *Chem. Mater.* 28 (2016) 127–134.
- [14] F. Fan, P. Kanjanaboos, M. Saravanapavanantham, E. Bearegard, G. Ingram, E. Yassitepe, M.M. Adachi, O. Voznyy, A.K. Johnston, G. Walters, G.H. Kim, Z.H. Lu, E.H. Sargent, Colloidal CdSe_{1-x}S_x nanoplatelets with narrow and continuously-tunable electroluminescence, *Nano Lett.* 15 (2015) 4611–4615.
- [15] Y. Zhou, M. Celikin, A. Camellini, G. Sirigu, X. Tong, L. Jin, K. Basu, X. Tong, D. Barba, D. Ma, S. Sun, F. Vidal, M. Zavelani-Rossi, Z.M. Wang, H. Zhao, A. Vomiero, F. Rosei, Ultrasmall nanoplatelets: the ultimate tuning of optoelectronic properties, *Adv. Energy Mater.* 7 (2017) 1602728.
- [16] J.R. Brent, D.J. Lewis, T. Lorenz, E.A. Lewis, N. Savjani, S.J. Haigh, G. Seifert, B. Derby, P.J. O'Brien, Tin (II) sulfide (SnS) nanosheets by liquid-phase exfoliation of herzenbergite: IV–VI main group two-dimensional atomic crystals, *J. Am. Chem. Soc.* 137 (2015) 12689–12696.
- [17] E. Izquierdo, A. Robin, S. Keuleyan, N. Lequeux, E. Lhuillier, S. Ithurria, Strongly confined HgTe 2D nanoplatelets as narrow near-infrared emitters, *J. Am. Chem. Soc.* 138 (2016) 10496–10501.
- [18] X. Li, J. Xia, L. Wang, Y. Gu, H. Cheng, X.M. Meng, Layered SnSe nano-plates with excellent in-plane anisotropic properties of Raman spectrum and photo-response, *Nanoscale* 9 (2017) 14558–14564.
- [19] X. Liu, Y. Li, B. Zhou, X. Wang, A.N. Cartwright, M.T. Swihart, Shape-controlled synthesis of SnE (E = S, Se) semiconductor nanocrystals for optoelectronics, *Chem. Mater.* 26 (2014) 3515–3521.
- [20] G. Almeida, S. Dogan, G. Berton, C. Giannini, R. Gaspari, S. Perissinotto, R. Krahne, S. Ghosh, L. Manna, Colloidal monolayer β -In₂Se₃ nanosheets with high photo-responsivity, *J. Am. Chem. Soc.* 139 (2017) 3005–3011.
- [21] L. Li, Z. Chen, Y. Hu, X. Wang, T. Zhang, W. Chen, Q. Wang, Single-layer single-crystalline SnSe nanosheets, *J. Am. Chem. Soc.* 135 (2013) 1213–1216.
- [22] S. Yuan, Y. Zhu, W. Li, S. Wang, D. Xu, L. Li, Y. Zhang, X. Zhang, Surfactant-free aqueous synthesis of pure single-crystalline SnSe nanosheet clusters as anode for high energy- and power-density sodium-ion batteries, *Adv. Mater.* 29 (2017) 1602469.
- [23] W.J. Baumgardner, J.J. Choi, Y. Lim, T. Hanrath, SnSe nanocrystals: synthesis, structure, optical properties, and surface chemistry, *J. Am. Chem. Soc.* 132 (2010) 9519–9521.
- [24] H. Chen, M. Lyu, M. Zhang, K. Feron, D.J. Searles, M. Dargusch, X. Yao, L. Wang, Switched photocurrent on tin sulfide-based nanoplate photoelectrodes, *ChemSusChem* 10 (2017) 670–674.
- [25] H. Ju, M. Kim, D. Park, J. Kim, A strategy for low thermal conductivity and enhanced thermoelectric performance in SnSe: porous SnSe_{1-x}S_x nanosheets, *Chem. Mater.* 29 (2017) 3228–3236.
- [26] R.G. Aswathy, Y. Yoshida, T. Maekawa, D.S. Kumar, Near-infrared quantum dots for deep tissue imaging, *Anal. Bioanal. Chem.* 397 (2010) 1417–1435.
- [27] G. Kucsko, P.C. Maurer, N.Y. Yao, M. Kubo, H.J. Noh, P.K. Lo, H. Park, M.D. Lukin, Nanometre-scale thermometry in a living cell, *Nature* 500 (2013) 54–58.
- [28] Y. Huang, L. Li, Y. Lin, C. Nan, Liquid exfoliation few-layer SnSe nanosheets with tunable band gap, *J. Phys. Chem. C* 121 (2017) 17530–17537.
- [29] C. Chowdhury, S. Karmakar, A. Datta, Monolayer group IV–VI monochalcogenides: Low-dimensional materials for photocatalytic water splitting, *J. Phys. Chem. C* 121 (2017) 7615–7624.
- [30] A. Kergommeaux, M. Lopez-Haro, S. Pouget, J. Zuo, C. Lebrun, F. Chandezon,

- D. Aldakov, P. Reiss, Synthesis, internal structure, and formation mechanism of monodisperse tin sulfide nanoplatelets, *J. Am. Chem. Soc.* 137 (2015) 9943–9952.
- [31] X. Tong, X. Kong, Y. Zhou, F. Navarro-Pardo, G.S. Selopal, S. Sun, A. Govorov, H. Zhao, Z. Wang, F. Rosei, Near-infrared, heavy metal-free colloidal “giant” core/shell quantum dots, *Adv. Energy Mater.* 8 (2018) 1701432.
- [32] L. Jin, B. Alotaibi, D. Benetti, S. Li, H. Zhao, Z. Mi, A. Vomiero, F. Rosei, Near-infrared colloidal quantum dots for efficient and durable photoelectrochemical solar-driven hydrogen production, *Adv. Sci.* 3 (2016) 1500345.
- [33] Y.-L. Lee, C.-F. Chi, S.-Y. Liao, CdS/CdSe co-sensitized TiO₂ photoelectrode for efficient hydrogen generation in a photoelectrochemical cell, *Chem. Mater.* 22 (2010) 922–927.
- [34] J.Y. Kim, Y.J. Jang, J. Park, J. Kim, J.S. Kang, D.Y. Chung, Y.E. Sung, C. Lee, J.S. Lee, M.J. Ko, Highly loaded PbS/Mn-doped CdS quantum dots for dual application in solar-to-electrical and solar-to-chemical energy conversion, *Appl. Catal. B-Environ.* 227 (2018) 409–417.
- [35] X. Tong, Y. Zhou, L. Jin, K. Basu, R. Adhikari, G.S. Selopal, X. Tong, H. Zhao, S. Sun, A. Vomiero, Z. Wang, F. Rosei, Heavy metal-free, near-infrared colloidal quantum dots for efficient photoelectrochemical hydrogen generation, *Nano Energy* 31 (2017) 441–449.
- [36] K. Ye, Z. Wang, J. Gu, S. Xiao, Y. Yuan, Y. Zhu, Y. Zhang, W. Mai, S. Yang, Carbon quantum dots as a visible light sensitizer to significantly increase the solar water splitting performance of bismuth vanadate photoanodes, *Energy Environ. Sci.* 10 (2017) 772–779.
- [37] Y.C. Qiu, S.F. Leung, Q.P. Zhang, B. Hua, Q.F. Lin, Z.H. Wei, K.H. Tsui, Y.G. Zhang, S.H. Yang, Z.Y. Fan, Efficient photoelectrochemical water splitting with ultrathin films of hematite on three-dimensional nanophotonic structures, *Nano Lett.* 14 (2014) 2123–2129.
- [38] J.S. Luo, L. Steier, M.K. Son, M. Schreier, M.T. Mayer, M. Gratzel, Cu₂O nanowire photocathodes for efficient and durable solar water splitting, *Nano Lett.* 16 (2016) 1848–1857.
- [39] F. Navarro-Pardo, H. Zhao, Z.M. Wang, F. Rosei, Structure/property relations in “giant” semiconductor nanocrystals: opportunities in photonics and electronics, *Acc. Chem. Res.* 51 (2018) 609–618.
- [40] S.S. Yi, J.M. Yan, Q. Jiang, Carbon quantum dot sensitized integrated Fe₂O₃@g-C₃N₄ core-shell nanoarray photoanode towards highly efficient water oxidation, *J. Mater. Chem. A* 6 (2018) 9839–9845.
- [41] H. Zhao, G. Liu, F. Vidal, Y. Wang, A. Vomiero, Colloidal thick-shell pyramidal quantum dots for efficient hydrogen production, *Nano Energy* 53 (2018) 116–124.
- [42] F. Formal, N. Tétreault, M. Cornuz, T. Moehl, M. Grätzel, K. Sivula, Passivating surface states on water splitting hematite photoanodes with alumina overlayers, *Chem. Sci.* 2 (2011) 737–743.
- [43] V.M. Nikolic, S.L. Maslovara, G.S. Tasic, T.P. Brdaric, P.Z. Lausevic, B.B. Radak, M.P. Marceta Kaninski, Kinetics of hydrogen evolution reaction in alkaline electrolysis on a Ni cathode in the presence of Ni–Co–Mo based ionic activators, *Appl. Catal. B-Environ.* 179 (2015) 88–94.
- [44] F. Navarro-Pardo, X. Tong, G.S. Selopal, S.G. Cloutier, S. Sun, A.C. Tavares, H. Zhao, Z.M. Wang, F. Rosei, Graphene oxide/cobalt-based nanohybrid electrodes for robust hydrogen generation, *Appl. Catal. B-Environ.* 245 (2019) 167–176.